

WFIRST/AFTA Coronagraph Technology Development

Milestone 1 Final Report

Reflective Shaped Pupil Mask Fabrication and Characterization

Bala K. Balasubramanian¹, Eric Cady¹, Pierre Echternach¹, N. Jeremy Kasdin², Brian Kern¹, John Krist¹, Richard Muller¹, Bijan Nemati¹, Keith Patterson¹, Ilya Poberezhskiy¹, A. J. Riggs², Dan Ryan¹, Victor White¹, Karl Yee¹, Hanying Zhou¹, Neil Zimmerman²

¹Jet Propulsion Laboratory, California Institute of Technology; ²Princeton University

January 16, 2015

1 OVERVIEW

In December 2013, NASA announced the selection of the Occulting Mask Coronagraph (OMC) as the primary architecture for the WFIRST/AFTA coronagraph instrument. OMC is a point design that is convertible between Shaped Pupil Coronagraph (SPC) and Hybrid Lyot Coronagraph (HLC) modes of operation. NASA set the objective of maturing the WFIRST/AFTA coronagraph to Technology Readiness Level (TRL) 5 by 9/30/2016. To this end, a technology development plan was drafted and approved that defined 9 milestones in fiscal years 2014-2016 that marked significant accomplishments on the path toward reaching TRL-5. The first key milestone was worded as:

“First-generation reflective Shaped Pupil apodizing mask fabricated with black silicon specular reflectance of less than 10^{-4} and $20\ \mu\text{m}$ pixel size,” with the due date of July 21, 2014.

The results submitted to WFIRST Study Office on June 16, 2014 and reviewed by the independent Technology Assessment Committee (TAC) on June 24, 2014 met both the nominal and substantive Milestone 1 success criteria, as was concurred by the TAC.

In regards to the nominal success criteria:

- Measured black silicon specular reflectance was $<10^{-7}$ vs. specular reflectance of $<10^{-4}$ called out in the milestone title.
- Pixel size was selected to be $22\ \mu\text{m}$ for the first generation mask, which has no impact on performance compared to the $20\ \mu\text{m}$ pixel size called out in the milestone title.

In regards to the substantive success criteria:

- Coronagraph contrast degradation attributable to all measured mask imperfections combined was assessed to have the upper bound of 3×10^{-10} .
- This estimated contrast degradation is acceptable for a coronagraph designed to perform well above 1×10^{-9} raw contrast level.
- The characterized mask was installed on the shaped pupil testbed in April of 2014 and used subsequently for the successful Milestone 2 starlight suppression demonstration.
- This upper bound was limited by the measurement sensitivity of one key testbed parameter, and the actual mask contribution to contrast degradation is likely significantly lower.

2 REFLECTIVE SHAPED PUPIL MASK MANUFACTURING

2.1 Shaped Pupil Fabrication Heritage Prior to WFIRST/AFTA

Over the past several years, shaped pupil masks for coronagraphs have been designed at the Princeton University's High Contrast Imaging Laboratory (HCIL) led by Professor Jeremy Kasdin and fabricated at JPL by a team led by Bala K. Balasubramanian. These shaped pupil masks were then tested both at Princeton's in-air coronagraph testbed and at JPL's vacuum High Contrast Imaging Testbed (HCIT). The masks were designed for an unobscured pupil and made to operate in transmission: they were produced as slits of various shapes in a thin silicon wafer with a Deep Reactive Ion Etching (DRIE) process [1]. An example of such a transmissive shaped pupil mask is shown in Figure 1.

The AFTA 2.4 meter telescope pupil with a central obscuration consisting of the secondary mirror and struts supporting it required completely new shaped pupil mask designs [2]. These new designs had fine "island" structures, so a free-standing transmissive mask presented major fabrication challenges. Therefore a transition to reflective mask fabrication technology was chosen to make the WFIRST shaped pupil masks. Using technology pioneered at JPL, reflective shaped pupil mask became feasible with islands of highly absorptive black silicon created on a silicon wafer coated with aluminum. In November 2013, an example of such a reflective mask with "island" features was produced for the first time at JPL (Figure 2) for an unobscured pupil design.

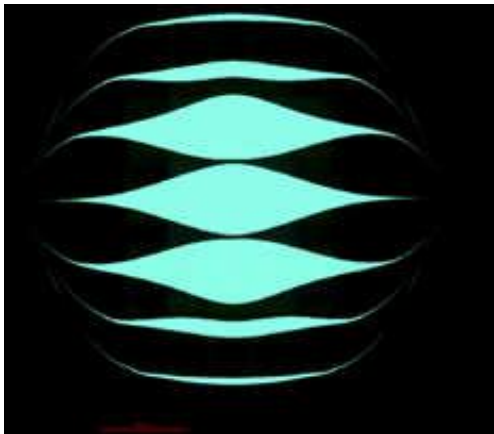


Figure 1. Example of a transmissive shaped pupil mask produced at JPL by Deep Reactive Ion Etching process for unobscured pupils.

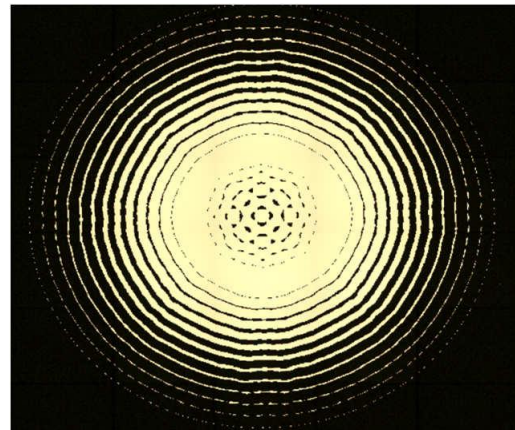


Figure 2. Example of a reflective shaped pupil mask on Al-coated silicon made for unobscured pupil.

2.2 Shaped Pupil Mask for WFIRST/AFTA Pupil

During the coronagraph downselect process in the Fall of 2013, HCIL at Princeton University designed two types of masks for the obscured AFTA telescope pupil:

1. Discovery mask that produces a 360° dark hole region with a fairly large inner working angle (IWA) exceeding $5\lambda/D$, where λ is the optical wavelength and D is the diameter of the telescope aperture. This type of mask will also be used for disc science.
2. Characterization mask for acquiring spectra of known exoplanets that produces a “bowtie-shaped” dark hole region with two ~60° parts. It has IWA of $\sim 4\lambda/D$ and deeper contrast at small working angles. Three such masks are sufficient to cover the entire field of view without rolling the telescope.

These shaped pupils that originated during the downselect process are referred to as “Generation 1” designs; they were finalized and delivered to JPL on January 31, 2014. Over a two month period from February to April 2014, the team at JPL refined the fabrication processes to produce such a reflective shaped pupil mask with e-beam lithography and black silicon technology, as described in the following section.

During the course of 2014, HCIL came up with improved SPC designs that reduced the inner working angle and increased coronagraph throughput, resulting in greater exoplanet science yield. These designs are referred to as “Generation 2” or SPLC (Shaped Pupil with Lyot-stop Coronagraph); they will be fabricated, characterized, and validated on the SPC testbed in 2015. From the fabrication perspective, which is relevant to this Milestone 1 report, Gen 2 shaped pupil designs are no more complex than Gen 1.

2.3 Reflective Shaped Pupil Mask Fabrication Process

Fabrication of reflective shaped pupil (RSP) masks meeting SPC performance requirements demands optimum choice of materials and processes, starting with the selection of silicon wafers and coatings. Some of the notable challenges are:

- Highly doped silicon wafers polished to a few angstroms RMS of surface finish and $< \lambda/10$ wavefront error on reflection over a 30 mm diameter area are long-lead custom items, since typical wafers for semiconductor applications are not produced to such requirements.
- Maintaining required Al coating reflectance uniformity after treatments of the wafer during black silicon processing requires careful protection of the reflecting regions.
- Achieving largely defect-free structures with ~20 micron minimum feature size.





Table I lists the key processing steps followed to produce the first generation RSP masks that meet WFIRST coronagraph performance requirements.

Table I. RSP mask fabrication and characterization steps

Process Step	Location / Tools	Comments
Shaped pupil mask design	Princeton University HCIL	Two design files delivered to JPL on 1/31/14: discovery and characterization
Wafer selection and procurement	Various	100 mm dia, 2 to 5mm thickness, <100> crystal plane, highly doped Si wafer, double side polished, $\lambda/10$ RMS WFE, <1 nm RMS roughness
Al coating	Precision Optical, Costa Mesa, CA	200 nm Al coating on Si wafer
Wavefront measurement	JPL / Zygo Interferometer	Choose coated wafer that meets wavefront error requirements
Data prep for fab	JPL	Prepared design data in required format for e-beam lithography at JPL; 4 RSP masks (35mm squares) on 100mm dia wafer for simultaneous processing
E-beam glass master	JPL / E-beam lithography of glass master	Chrome-on-glass master with mask patterns
Expose patterns on Al coated wafer	JPL / Lithography tools at JPL's MicroDevices Lab (MDL)	Wafer with patterns ready for cryo-etching black silicon structures
Cryo etching of black silicon structures on the patterned wafer with protected Al regions	Caltech Kavli Nanoscience Institute (KNI) / ICP cryo etcher	Cryo-etched wafer ready for removing the protective layer on Al and dicing of individual masks
Dicing of mask chips and removal of protective photo resist to expose Al	JPL / Wafer dicing tool	Diced and separated 4 masks; ready for inspection.
Imaging of mask features, defects	JPL / Nikon microscope	Detailed high resolution images of masks and defects, if any, for modeling and evaluation
Al reflectance measurement	JPL / Perkin Elmer 1050 spectrophotometer	Measured reflectance of Al regions over the band of 400 nm to 900 nm in 2nm intervals
Black Si diffuse reflectance measurement	JPL / PE1050 spectrophotometer with integrating sphere	Measured total integrated hemispherical reflectance (specular + diffuse) of black silicon from 400 nm to 1000 nm
Black Si specular reflectance measurement	JPL / custom setup to measure specular reflectance	Measured specular reflectance of black silicon at 8 deg AOI with 633nm laser

2.4 RSP Masks Delivered to SPC Testbed

High quality masks fabricated during March 2014 were delivered to the SPC coronagraph testbed. Full images of these two masks are shown in Figure 3, central portion of the characterization mask is shown in Figure 4(a), while Figure 4(b) shows a zoomed-in image revealing 22 micron minimum mask feature size.

	
<p>Figure 3a. Microscope image of a characterization mask. Faint grid structure is due to image stitching artifacts of >200 sub-images. Colored tint is due to microscope illumination.</p>	<p>Figure 3b. Microscope image of a discovery mask. High resolution images have been examined and used for modeling the impact of defects on performance</p>
	
<p>Figure 4a. Features in the central region of the characterization mask shown in figure 3a.</p>	<p>Figure 4b. High resolution image showing 22 μm minimum feature size.</p>

Inevitably, even a high quality fabricated mask has various imperfections when compared to the ideal designed mask. Much effort went into characterizing and quantifying different types of mask imperfections, as well as modeling and analysis to assess the impact of each imperfection type on coronagraph performance. The next section of this report describes this work in detail.

3 MASK IMPERFECTIONS AND THEIR IMPACT ON CORONAGRAPH PERFORMANCE

3.1 Black Silicon Reflectance

3.1.1 Impact of black silicon reflectance – analysis

Black silicon process developed at JPL uses a cryogenic reactive ion etching (CRIE) system to create sub-micron needle structure on the silicon surface. This structure modifies the effective refractive index of the medium and achieves remarkably low broadband reflectance combined with high absorption in the silicon by means of multiple bounces. The “blackness” of this material has been improved significantly over the years as a result of process optimization. Figure 5 shows the nanostructure of the silicon surface after CRIE.

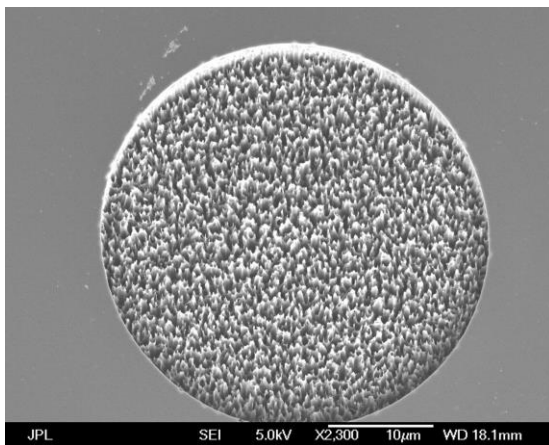


Figure 5a. SEM image of typical black Si surface

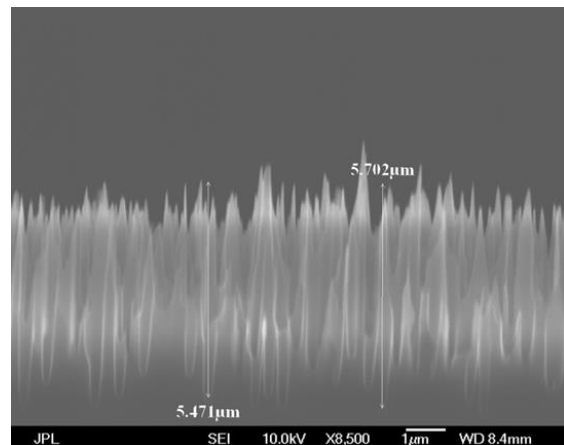


Figure 5b. SEM cross section image of typical black Si surface

In radiometry, the reflectance of a surface is divided into two components, specular and diffuse. The specular reflectance component is that expected from a “smooth” surface, where Fresnel reflection coefficients and calculations of optical path length to the surface determine its imaging qualities (e.g. a typical flat mirror). The diffuse reflectance component is a product of the “roughness” of the surface, where optical path lengths undergo large excursions. The diffuse reflected light is assumed to follow a characteristic distribution in emergent angle, nominally Lambertian in the absence of a more detailed understanding. The wavefronts associated with

diffuse reflectance have mutual coherence functions representing OPDs of a substantial fraction of the illuminated diameter, which for all practical purposes is incoherent for all but laser-line illumination.

In the context of the SPC, the treatments of the specular and diffuse reflectance of the black Si follow very different analyses. The treatment of the specular reflectance follows a similar analysis to that of the coronagraph itself, with a different “input” illumination. The left-hand panel of Fig. 6 shows the input illumination of the SPC, from the Al reflection (the desired SPC response) and from the specular reflectance of the black Si. The black Si specular reflectance can be quantified by a value R_s , with $0 \leq R_s \leq 1$.

The processing that creates the black Si depresses the height of the black Si surface by a distance on the order of $10 \mu\text{m}$, relative to the location of the Al surface. At this distance, for all but very narrow bandpasses ($\Delta\lambda/\lambda < 5\%$), the wavefront reflected from the Al and that specularly reflected from the black Si are mutually incoherent with respect to each other. As such, the PSF from specular reflection off the Al and the PSF from specular reflection off the black Si do not interfere, but rather add by intensities. The two PSFs are shown in the left-hand panel of Fig. 6. The brightness of the black Si PSF in the dark hole region is shown in the right-hand panel of Fig. 6, for $R_s=1$, normalized by the Al PSF peak I_0 . For any real value of R_s , the contribution of the black Si PSF to the dark hole is the curve on the right-hand panel of Fig. 6, multiplied by R_s .

The performance of the SPC is most closely tied to the contrast performance near the coronagraph inner working angle, which is $\sim 4 \lambda/D$ for this design. From the right-hand panel of Fig. 6, the black Si contribution in the neighborhood of $4 \lambda/D$ is approximately 3×10^{-3} . Thus, to keep the black Si contribution to acceptable levels, e.g. $< 3 \times 10^{-10}$ at $4 \lambda/D$, a specification of $R_s < 10^{-7}$ is needed.

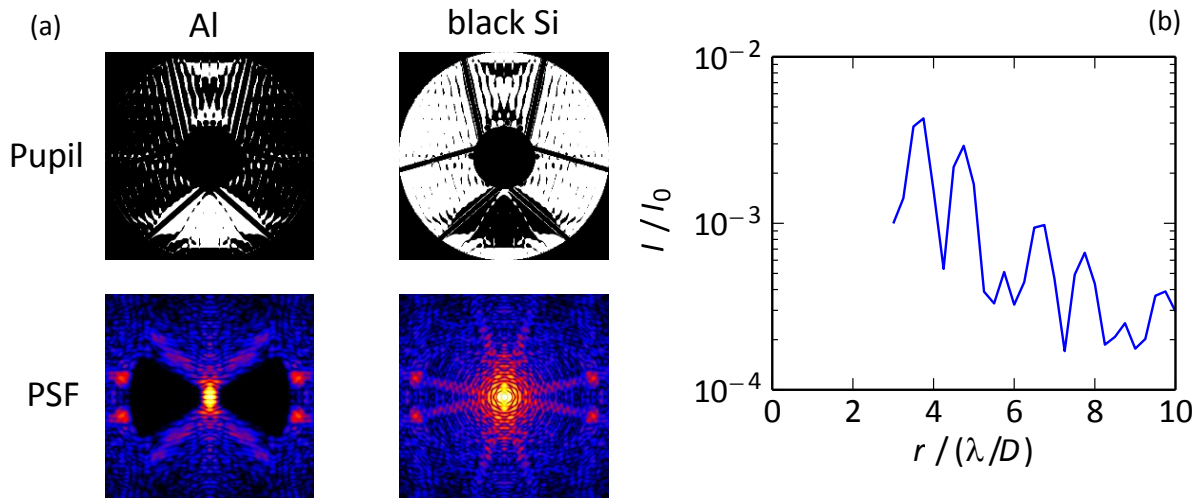


Fig. 6. (a) Pupil-plane distributions of specular reflection from Al and black Si surfaces, and the resulting PSFs, and (b) the image-plane intensity in the dark hole region as a function of radius for the black Si specular reflectance, normalized by the peak Al PSF brightness (I_0), for $R_s=1$.

The diffuse reflectance of the black Si creates a near-uniform illumination of the dark hole region, mutually incoherent with respect to the PSF reflected off the Al. The scattering angles at the shaped pupil that correspond to the dark hole region at the science camera are measured in units of (λ/D_{SP}) , which for $\lambda = 550 \text{ nm}$, $D_{SP} = 22 \text{ mm}$,

$$\lambda/D_{SP} = 2.5 \times 10^{-5} \text{ rad}$$

The Lambertian distribution is $I \propto \cos(\theta)$, meaning that it varies on angular scales of radians. The diffuse reflected light can be considered to be constant at $I/I_{in} = R_d/\pi \text{ ster}^{-1}$ out to $\gg 1000 \lambda/D$, where R_d is the diffuse reflectance, $0 < R_d < 1$. From dimensional arguments alone, it could be expected that $I/I_0 \sim (\lambda/D_{SP})^2 \sim 10^{-9} R_d$. Calculating the fraction of the illuminated pupil occupied by black Si (as opposed to Al), and normalizing to the peak Al PSF intensity, the proper comparison of intensities produces

$$I/I_0 = 1.3 R_d \times 10^{-9}$$

Thus, a specification of $R_d < 1\%$ limits the diffuse reflectance contribution to the contrast in the dark hole to 1.3×10^{-11} .

3.1.2 Measurement of black silicon reflectance

Measurements of the total (diffuse + specular) reflectance of black silicon were made with a Perkin Elmer 1050 spectrophotometer fitted with an integrating sphere. The samples – both the device under test and a calibrated reference – were installed at the same 8° angle of incidence as in the coronagraph testbed. Figure 7 shows the schematic of this measurement, while the results are shown in Figure 8.

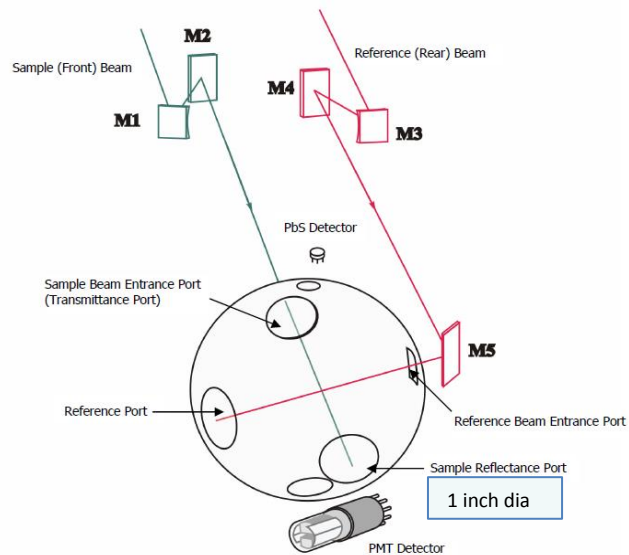


Figure 7. Optical schematic of the integrating sphere measurement with PE1050 spectrophotometer

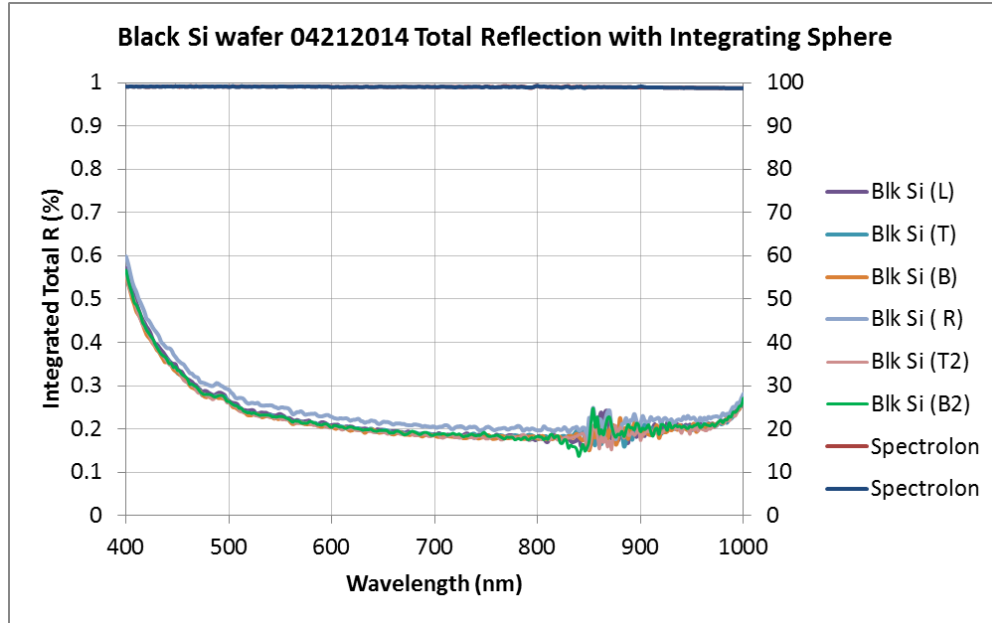


Figure 8. Total hemispherical reflectance (specular + diffuse at 8 deg AOI) of a black silicon sample measured with an integrating sphere on a PE 1050 spectrophotometer, calibrated with LabSphere Spectrolon™ reference standard. Noise beyond 850 nm is due to a detector change in the system.

The commercial spectrophotometer, however, did not have the sensitivity to measure the specular reflectance of black silicon, which, as was analytically shown in Section 3.1.1, can potentially have a significant impact on SPC contrast. In order to measure this critical parameter, we built a dedicated laboratory setup shown in Figure 9.

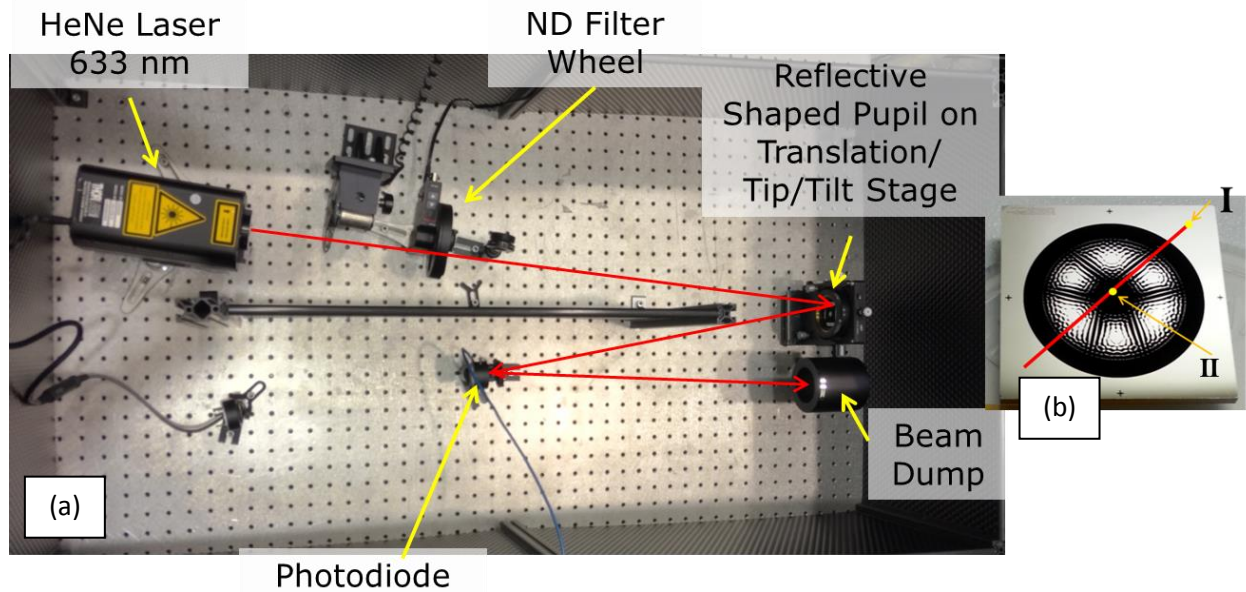


Figure 9. (a) A dedicated lab setup for measuring black silicon reflectance. Neutral density filters (OD 1 to OD 6) extend the dynamic range and allow measurement calibration. (b) Translating the sample between aluminum-coated (I) and black silicon (II) regions calibrates out common-mode testbed losses.

The setup uses a HeNe laser with 633 nm wavelength whose collimated output beam passes through a wheel with several neutral density (ND) filters and is reflected off a shaped pupil mask under test. The mask has both highly reflective aluminum-coated regions and black silicon regions and can be translated transversely so that laser light hits either of the two regions, as shown in Fig. 9b. The detector (either a discrete photodiode or a digital camera) is centered on the specular reflection of the beam when the laser light hits the aluminum. The optical powers reflected from the aluminum-coated region and black silicon region are then compared. A series of studies was performed with the detector moved transversely to and along the beam to separate diffuse and specular components. The setup is fully enclosed to minimize the ambient light leakage.

The ability to put ND filters from OD 1 to OD 6 in the optical path extends the measurement dynamic range and allows performing a calibration of the measurement accuracy. Newport 818-SL detector and Newport 1830-C low-noise power meter were used in the measurement. The most conservative measured value of the specular reflectance was $R_s = 7 \times 10^{-8}$. This value was limited by the measurement setup sensitivity and the real value is likely to be significantly lower. In fact, the reflection off black silicon shows no prominent specular component, as shown in Figure 10 taken with a WinCamD camera.

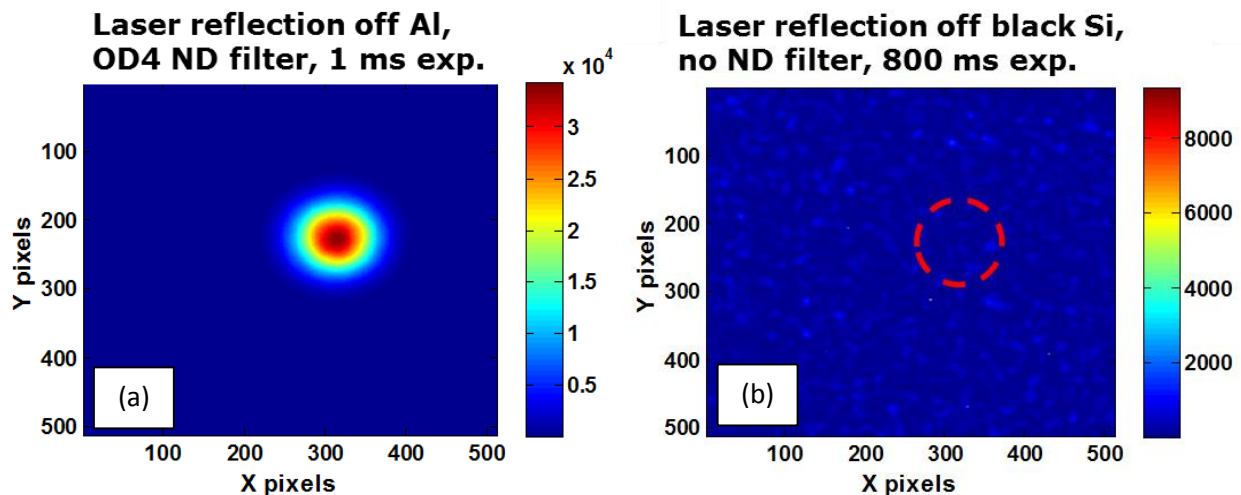


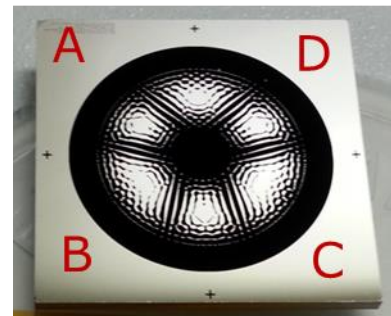
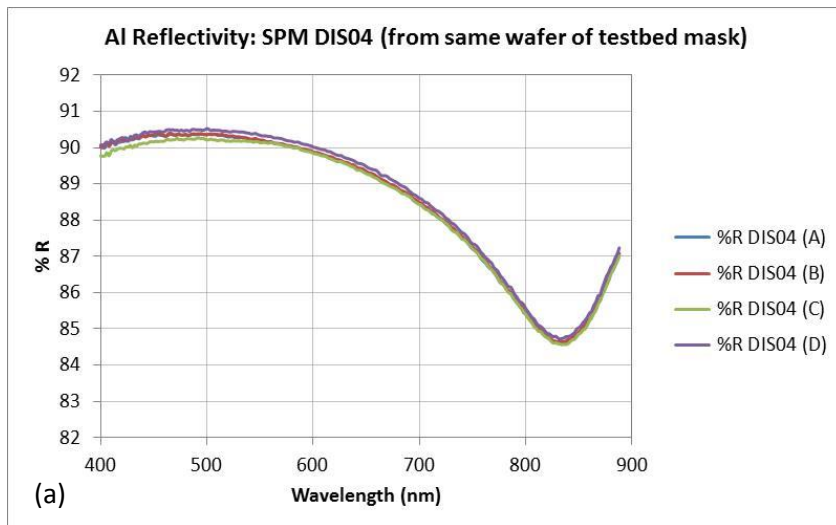
Figure 10. Comparison of camera images with laser beam reflecting off (a) aluminum coated region and (b) black silicon region. Speckle morphology of black Si reflection shows no detectable specular reflection peak.

Putting together the sensitivities derived in section 3.1.1 and the measurement results described in section 3.1.2, we get the following contrast degradation in the dark hole expected due to black silicon reflectance:

- Specular reflectance: $I/I_0 = 7 \times 10^{-8} \times 3 \times 10^{-3} = 2.1 \times 10^{-10}$
 - This is an upper bound limited by the measurement sensitivity, actual contribution is likely to be substantially lower.
- Diffuse reflectance: $I/I_0 = 0.006 \times 1.3 \times 10^{-9} = 8 \times 10^{-12}$
 - Used value of $R_d = 0.6\%$ is highly conservative, as black silicon $R_d < 0.3\%$ above 450 nm (Figure 8).

3.2 Aluminum Reflectance Variations

The Perkin Elmer 1050 spectrophotometer was also employed to measure the reflectance of aluminum areas on the masks over the spectral range from 400nm to 900nm. Figure 11 shows the reflectance curves at 4 mask locations. Aluminum reflectance variation across the mask is small and consistent with other witness samples produced along with testbed mirrors during the coating process. This demonstrates that aluminum coating was well protected by photoresist during the black silicon process, so that finished RSP masks have similar Al coating quality to other coronagraph optics, such as OAPs and fold mirrors.



(b)

Figure 11 (a) Reflectance of Al regions on the fabricated mask, measured at 8° AOI with PE1050 spectrophotometer; (b) 4 locations on the mask where the Al reflectance was measured.

The impact of aluminum reflectance variations on contrast can be analyzed based on a previously derived analytic model [3]. Referring to Fig. 12, consider an optic having a weak periodic surface deformation of N cycles across a beam of diameter D , with rms surface height s , reflectance (amplitude) rms $A \ll 1$ and phase amplitude $\alpha \ll 1$ radians. Collimated light reflects from the surface, propagates a distance z to the pupil (or pupil conjugate) plane with a wavefront corrector (deformable mirror) DM_p , and then reaches to second deformable mirror DM_{np} . The optical surface reflectance variation (amplitude modulation) would then cause two main effects:

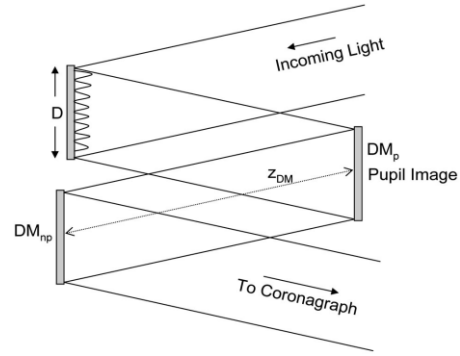


Figure 12. 2-DM coronagraph configuration

- Zero-order (amplitude) effect, which is fully correctable with DM amplitude control using DM stroke given as:

$$s_{DM} = D^2 r / 8\pi^2 z_{DM} N^2$$

where D is the beam diameter; r is the reflectance non uniformity; z_{DM} is the distance between two DMs, and N is the spatial frequency in cycles/aperture.

- First-order (amplitude-to-phase cross coupling) propagation effect, which is not fully correctable over bandwidth with DM phase control; the residual contrast is proportional to the propagation distance to DM:

$$C = \frac{1}{6R^2} \cdot \left(\frac{\pi r z \lambda_o N^2}{2D^2} \right)^2$$

where R is the spectral resolution, and z is the propagation distance to (pupil) DM.

For the shaped pupil mask located at a pupil plane, there is no first order effect, while the zero order amplitude effect can be fully corrected using just a fraction of the available DM stroke. In our case, the measured reflectance nonuniformity is $r \sim 1\%$, $N = 4$, $D = 22\text{mm}$, $Z_{DM} = 1\text{m}$. **Thus, the DM stroke needed to fully correct RSP mask Al coating reflectance nonuniformity is $s_{DM} \sim 4$ nm peak-to-valley, which is $<1\%$ of DM stroke available in the baselined AOX DMs.**

3.3 Isolated Mask Defects

Since the RSP mask is at a pupil plane, it is expected to be rather tolerant of manufacturing defects such as minor scratches in black silicon and aluminum after DM wavefront control is applied. This was confirmed by simulations performed using SPC PROPER model for the installed mask with as-measured defects.

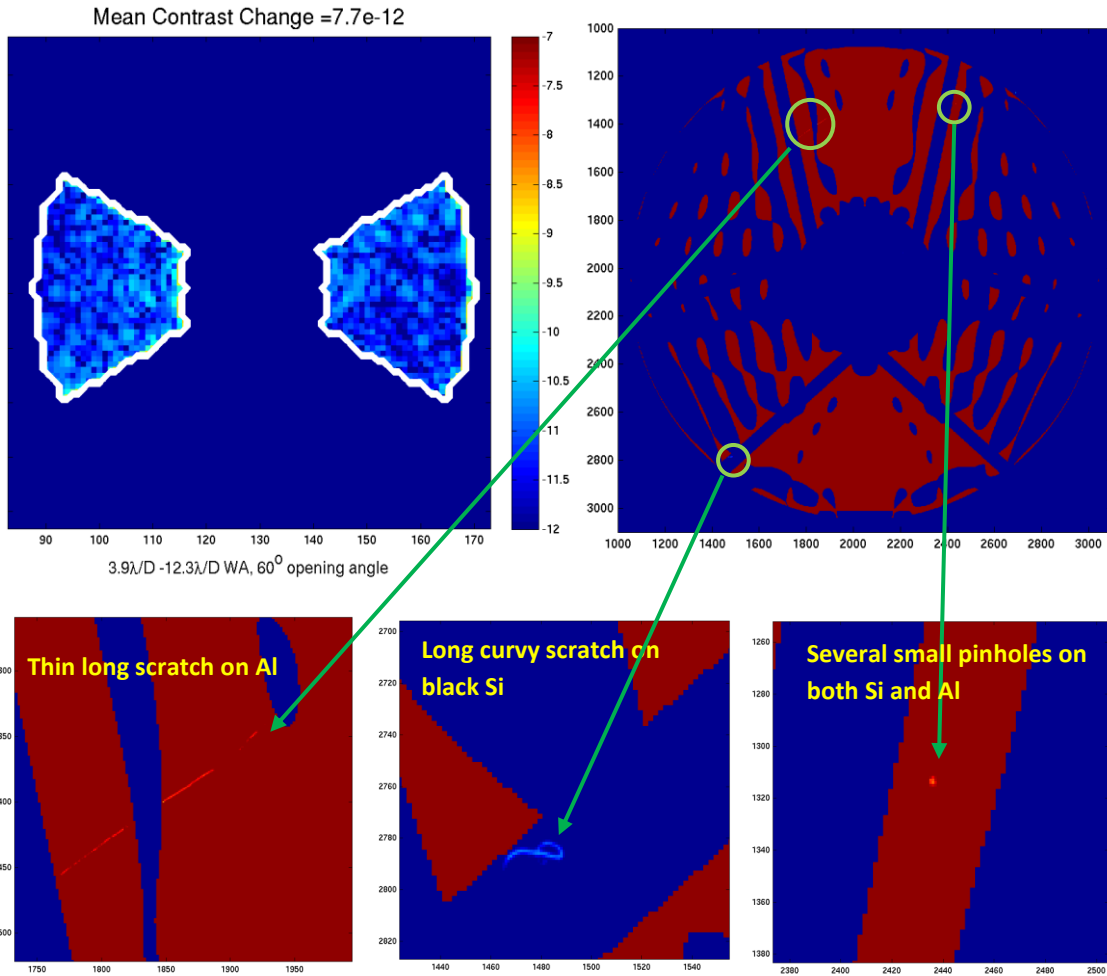


Figure 13. Notable mask defects implanted in the model and the mean contrast change they caused.

The defects identified from high resolution images of the fabricated mask are about half dozen small spots of 10~30 μm in size on either black Si or Al. Additionally, there is one thin scratch of about 0.5mm in length on Al, and another ~100μm length curvy scratch on black Si (Figure 13). To model the impact of these defects on SPC contrast, the original design mask of 1000x1000 pixel size (22mm diameter physical size) was block up-sampled to 2000x2000 pixel size for a resolution about ~10μm/pixel (even larger resolution would be preferable, but is currently limited by EFC calculation speed). Post-EFC wavefront control contrast was then calculated. Defects observed in the high resolution scanned manufactured mask were then implanted into the model and post-EFC contrast was recalculated. **The mean contrast change due to isolated mask defects after wavefront control is 7.7×10^{-12} .**

3.4 Mask Wavefront Error

Wavefront error of the RSP mask in its testbed mount was measured using a Zygo interferometer. In principle, the low order RSP mask surface errors are fully correctable with a pupil plane DM. However, due to discreteness of DM actuators, this correction may not be

smooth if large DM strokes are needed for significant correction. This will result in residual wavefront error that requires further EFC wavefront control. The impact on contrast due to SP mask surface error (or its DM corrected residual wavefront error) was modeled using PROPER diffraction model with EFC control.

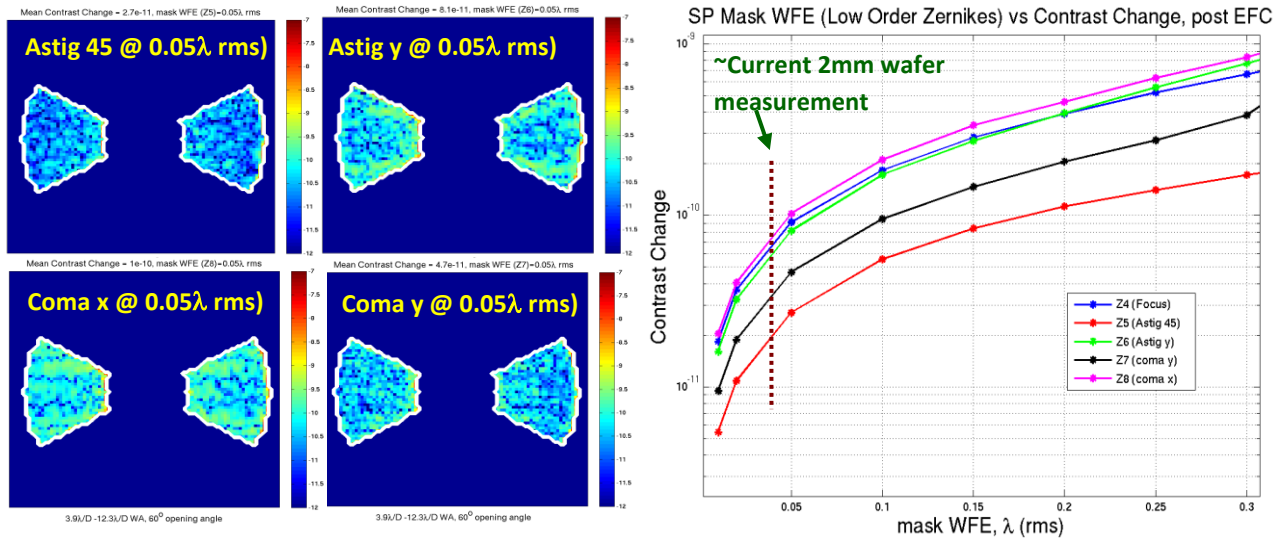


Figure 14. (a) Contrast change for mask WFEs of 0.05 λ rms for Zernike terms Z5~Z8. (b) Contrast change vs low order Zernike term mask WFE.

First, post EFC control contrast for the designed SP mask was obtained. Then low order Zernike wavefront error terms of interest (Z4 – Z8) were added to the SP mask design, one at a time, ranging from 0.01 to 0.3 λ rms. Before applying EFC control, the pupil plane DM1 was fitted to the WFE to get its initial setting, simulating the correction of low order mask WFE. We then evaluate post-EFC control contrast for each case. The results are shown in Figure 14. In general, the contrast change due to individual Zernike term WFE is less than 10⁻¹⁰ if the term is smaller than 0.05 λ rms.

For the SP mask installed in the testbed, WFE of 19.6 nm rms was measured, or 0.036 λ rms after removing the focus term (which is accommodated during alignment by translating the field stop). **The upper bound on the post EFC contrast deterioration due to RSP mask wavefront error is 7×10⁻¹¹.**

4 SUMMARY

A reflective shaped pupil coronagraph mask designed for the WFIRST/AFTA telescope was fabricated and extensively characterized. Each known mask imperfection type was measured and the resulting coronagraph contrast degradation was quantified, as summarized in Table II. The reported total impact on contrast is a conservative upper bound, dominated by black silicon specular reflectance measurement sensitivity. Thus, the true contrast degradation due to the mask is likely to be significantly lower.

This conservatively assessed impact of mask imperfections on contrast – 3×10^{-10} – is acceptable for the WFIRST/AFTA coronagraph shaped pupil mode that was designed to produce raw contrast over 10 times lower. Thus Milestone 1 success criteria were met; as was concurred by the TAC and validated when the shaped pupil testbed subsequently demonstrated high contrast in both narrowband and broadband light using the characterized mask.

Table II. Mask imperfections and their impact on SPC contrast.

Mask Imperfection Type	Measured Level	Impact on contrast after WF control	Comments
Black silicon reflectivity, specular	$<7 \times 10^{-8}$	$<2.1 \times 10^{-10}$	Upper bound only (no detection); limited by measurement setup
Black silicon reflectivity, diffuse	$<0.6\%$	$<10^{-11}$	
Mask WFE	$\sim 0.036 \lambda$ rms (above focus)	7×10^{-11}	- Post WF control - Better wafers received for future masks
Isolated defects	Several small pinholes and 2 scratches	8×10^{-12}	Post WF control
Aluminum reflectivity variations	$\sim 0.5\%$	fully correctable	Post WF control, not including chromatic effects
Total		$<3 \times 10^{-10}$	Upper bound

5 ACKNOWLEDGEMENT

Parts of this research were carried out at the Jet Propulsion Laboratory, California Institute of Technology, under a contract with the National Aeronautics and Space Administration. Copyright 2015. All rights reserved.

6 REFERENCES

1. K. Balasubramanian, D. Wilson, V. White, R. Muller, M. Dickie, K. Yee, R. Ruiz, S. Shaklan, E. Cady, B. Kern, R. Belikov, O. Guyon, N. Jeremy Kasdin, "High contrast internal and external coronagraph masks produced by various techniques," Proc. SPIE 8864, (2013)
2. A.J. Riggs, N. Zimmerman, A. Carlotti, N.J. Kasdin, R. Vanderbei, "Shaped pupil design for future space telescopes," Proc. SPIE 9143, 9143-69, (2014)
3. S. B. Shaklan and J. J. Green, "Reflectance and optical surface height requirements in a broadband coronagraph. 1. contrast floor due to controllable spatial frequencies," Appl. Opt., vol. 45, no. 21, pp. 5143-5153 (2006)

APPENDIX A: LIST OF ACRONYMS

AFTA	Astrophysics Focused Telescope Assets
AOI	Angle of Incidence
AOX	Northrop Grumman's AOA Xinetics
CRIE	Cryogenic Reactive Ion Etching
DM	Deformable Mirror
DRIE	Deep Reactive Ion Etching
EFC	Electric Field Conjugation (wavefront control approach used in HCIT)
HCIL	High Contrast Imaging Laboratory (at Princeton University)
HCIT	High Contrast Imaging Testbed (at JPL)
IWA	Inner Working Angle
JPL	Jet Propulsion Laboratory
KNI	Kavli Nanoscience Institute (at Caltech)
MDL	MicroDevices Laboratory (at JPL)
NASA	National Aeronautics and Space Administration
ND	Neutral Density
OAP	Off-Axis Parabola
OD	Optical Density
OMC	Occulting Mask Coronagraph
RSP	Reflective Shaped Pupil (mask)
SPC	Shaped Pupil Coronagraph
TAC	Technology Assessment Committee
TDEM	Technology Development for Exoplanet Missions
TRL	Technology Readiness Level
WFE	Wavefront Error
WFIRST	Wide-Field Infrared Survey Telescope